Supplementary information: Lifetime of interlayer breathing modes of few-layer $2H$-$MoSe_2$ membranes.

P. Soubelet,[1] A. A. Reynoso,[1] A. Fainstein,[1] K. Nogajewski,[2,3]
M. Potemski,[2,3] C. Faugeras,[3,*] and A. E. Bruchhausen[1,†]

[1] *Centro Atómico Bariloche & Instituto Balseiro (C.N.E.A.) and CONICET, 8400 S.C. de Bariloche, R.N., Argentina.*
[2] *Institute of Experimental Physics, Faculty of Physics, University of Warsaw, Pasteura 5, 02-093 Warsaw, Poland.*
[3] *Laboratoire National des Champs Magnétiques Intenses (CNRS, UJF, UPS, INSA), BP 166, 38042 Grenoble Cedex 9, France.*

(Dated: 24th April 2019)

This supplementary information extends some points discussed in the main text, and presents additional data that could be of interest for some readers. Section I discusses the sample, addressing how the "free-standing" (unsupported) samples are distinguished. The processing and analysis of the measured $\Delta R/R$ transients are explained in section II. The reason for the chosen pump-probe fluence used in the experiment is explained in section III. Section IV provides a brief description of the linear chain model used to describe the vibrational modes in combination to additional Raman experiments in few-layer $MoSe_2$ to derive the out-of-plane acoustic sound velocities. The particular case of the thicker bulk-like samples, their analysis and simulations are described in section V. In sections VI A and VI B we address the two models used to simulate and fit the scattering decay rates of acoustic phonons in bulk $MoSe_2$, briefly discuss their limitations in VI C, and in section VI D some considerations related to the surface roughness phonon decay mechanism, of critical importance for the thinner samples, are analysed. Finally, a brief analysis of the quality factor of the B_1 modes, assumed as a simple mechanical oscillator, is presented in section VII.

* E-mail: clement.faugeras@lncmi.cnrs.fr
† E-mail: Axel.Bruchhausen@cab.cnea.gov.ar

CONTENTS

I. SAMPLE ADDRESSING

The exfoliated $MoSe_2$ flakes are scattered on a 90 nm SiO_2/Si substrate wafer, which has been previously patterned with regular circular holes of $\sim$6 μm in diameter. As a result, some flakes were randomly deposited on top of the holes, and were therefore only supported by the holes' borders, i.e. were in a "free-standing" condition.

To ensure the correct addressing of the spot on top of the samples, our experimental system allows to acquire simultaneously the white light image and the time-resolved measurement. Figure S-1 on the left, shows the optical microscope images for a 22L $MoSe_2$ flake through the 100× objective, where the laser spot is clearly observed next to a patterned hole (Fig. S-1a, left), and centred on top of this hole (Fig. S-1b, left). The corresponding measured transient reflectivity $\Delta R/R$, for each condition, is shown on the respective right panels. The origin of the observed

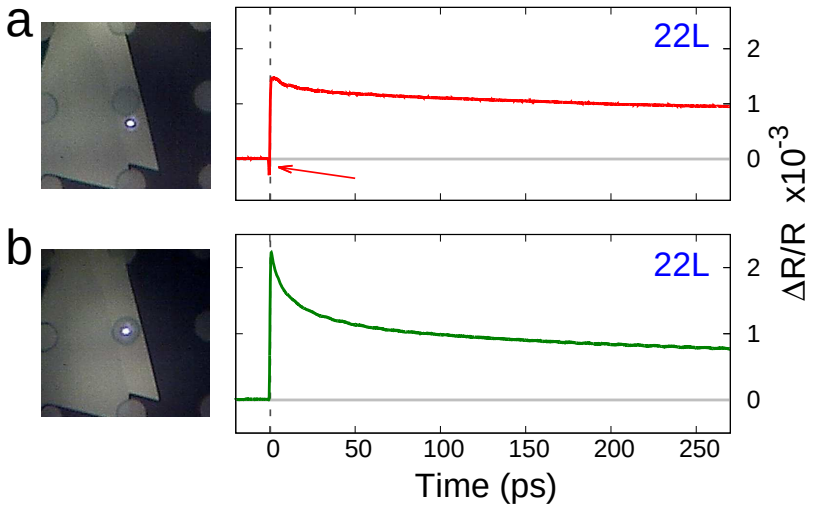

Figure S-1. Typical "as measured" transient reflectivities $\Delta R/R$ for a supported sample (**a**) and a suspended sample (**b**). The optical images left to the transients, taken through the 100× objective, show the precise addressing of the laser spot on top of the sample for the respective cases.

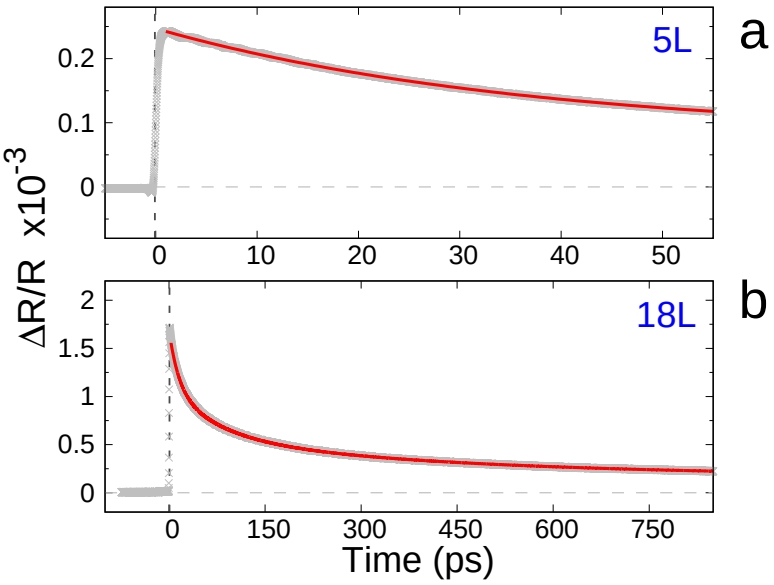

Figure S-2. As measured $\Delta R/R$ transient for samples with 5L $MoSe_2$ (**a**) and 18L $MoSe_2$ (**b**). The grey symbols correspond to the measurement and the red curves are the multi-exponential fitting. For the 18L sample the sum of three decaying exponentials was needed to fit the experiment, while for the 5L sample only one decaying exponential was enough to well describe the curve.

transient signal is mainly due to the changes in the optical constants resulting from the impulsively modified electronic states within the samples at $t = 0$, i.e. at the arrival of the pump pulse.

Both transient signals are relatively strong, but evidently different for each of the situations. On top of the hole, the onset (at $t = 0$) changes abruptly from its unperturbed position towards positive values (Fig. S-1b, right) and relaxes back towards its equilibrium. Besides the hole, within the first few picoseconds, the transient reflectivity has an initial impulsive deflection towards *negative* values (see the arrow in Fig. S-1a, right), and rapidly changing to positive values. This initial negative impulsive deflection, the slightly lower initial positive value reached before the signal's quasi-exponential decay towards equilibrium, and the smaller exponential decay are a systematic behaviour displayed by the transients obtained for the supported flake, and is a fingerprint -in addition to the optical image- that enables unambiguously to distinguish in which situation we are, i.e. if the spot is on a supported or suspended (free-standing) position in the flake.

II. SIGNAL PROCESSING

Figure S-2 shows the untreated ("as measured") $\Delta R/R$ transient for 5L and 18L $MoSe_2$, panels a) and b) respectively. The contribution to the transient reflectivity due to the phonon modes in the sample needs to be extracted by subtracting a fitted multi-exponential function, where the exponential decay constants are related with electronic processes, such as the decay of excitons and intervalley scattering, or exciton dephasing [1]. The red curves in the figure S-2 are the corresponding multi-exponential fittings and show a good agreement with the experiment. It is important to point out that the measured temporal window for each experiment was modified depending on the phonon dynamics, extending the window when the phonon lifetime was longer, reducing the relative noise of the measurement. To perform the fitting, we used the sum of up to three decaying exponential functions to have the best possible description, and consequently the cleanest contribution of the phonon mode oscillations. For the sample with 5L a single exponential is enough to well fit the decay ($\tau_1 \simeq 37\,\text{ps}$). For the sample with 18L, three exponential functions were needed to describe the curve. For the later case, the best agreement was found using: $\sum_{m=1}^{m=3} A_m \exp(-t/\tau_m)$, with $\frac{A_2}{A_1} = 0.890$, $\frac{A_3}{A_1} = 0.711$, $\tau_1 = 14.8\,\text{ps}$, $\tau_2 = 75.3\,\text{ps}$, and $\tau_3 = 432\,\text{ps}$.

The extracted oscillations for the samples with 5L is shown in Figure 2 of the main text, and for the case of the 18L $MoSe_2$ sample, the result and consequent treatment obtained after the subtraction process described above is shown in Fig.S-3.

The filtered phonon contribution to the transient is displayed in Fig.S-3a. It is possible to clearly observe the

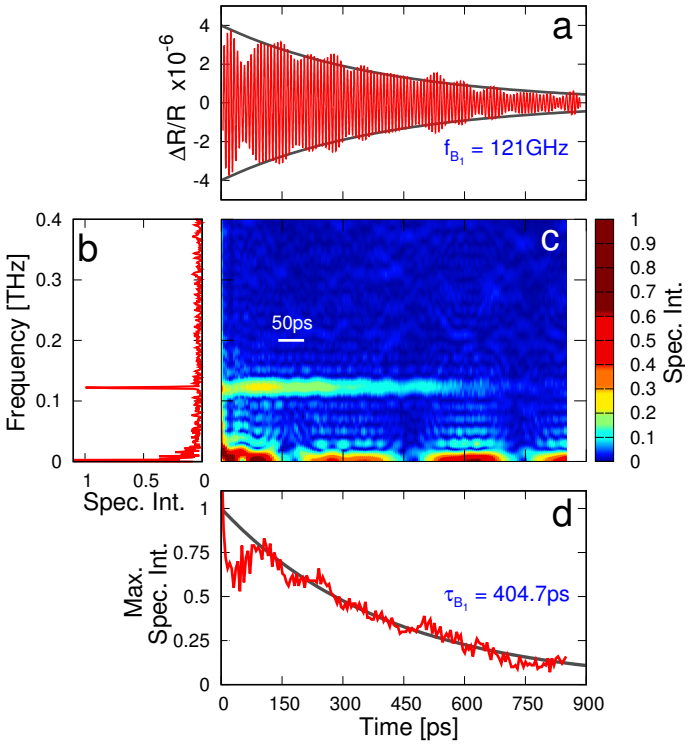

Figure S-3. Signal processing for 18L $MoSe_2$. **a)** filtered $\Delta R/R$ (red) and fitted exponential decay envelope (grey). **b)** numerical Fourier transform of $\Delta R/R$. **c)** density map of the wnFT of the phonon signal $\Delta R/R$ (gliding window 50 ps). **d)** B_1 mode's intensity extracted from the density map of the wnFT (red) and fitted exponential decay (grey).

decrease of the acoustic oscillation's amplitude associated to the phonon damping. The exponential envelope is indicated (gray curve) and a τ_{B_1} of 404.7 ps is obtained.

The spectral components of this signal can be better analyzed by performing the numerical Fourier transform (nFT), which is presented in Fig.S-3b. The spectrum displays a *single* peak at ∼121 GHz corresponding to the B_1 mode of the suspended flake. To have a hint of the temporal dynamics in the spectral domain, a windowed numerical Fourier transform (wnFT) is presented in Fig.S-3c. This wnFT was performed using a gliding window of 50 ps, as indicated in the figure. This density plot shows the behavior of the intensity of each spectral components and its evolution in time. The intensity of the B_1 mode at ∼121 GHz decreases exponentially, vanishing below the noise level. Figure S-3d displays the B_1 mode intensity extracted from the density map of the wnFT together with the same exponential envelope presented in panel a) and yielding the same acoustic exponential decay time. The low frequency noise appearing in Fig.S-3c for frequencies $\leq$ 25 GHz, are probably an artifice that remains from subtracting the electronic contribution.

III. PUMP LASER FLUENCE DEPENDENCE

All the transient reflectivity pump-probe measurements presented were performed with a 100× objective of NA=0.90, that was used to focus the laser down to a spot of ∼1 μm diameter. Figure S-4 shows the pump laser fluence dependence of the spectral intensity of the fundamental mode, for a 22 layer $MoSe_2$. The blue vertical arrow indicates the fluence of the probe laser used in all the measurements, which was set to 0.16 mJ/cm^2. As observed, the phonon intensity grows rather linearly with the generating incident power until its maximum at about ∼1.20 mJ/cm^2. When further increasing the pump power, the spectral intensity saturates and decreases afterwards until ∼3 mJ/cm^2, where the sample breaks. The red dashed line indicates the approximately linear within the initial range. The pump fluence used in the experiments for the phonon lifetime determination, is marked by the red arrow, and was set to 0.64 mJ/cm^2. It was chosen to be significantly larger than the probe power, but far enough from the saturation. The pump-probe fluence ratio (4:1) is coincidently similar to those values used in other reported works for experiments that are alike [1, 2].

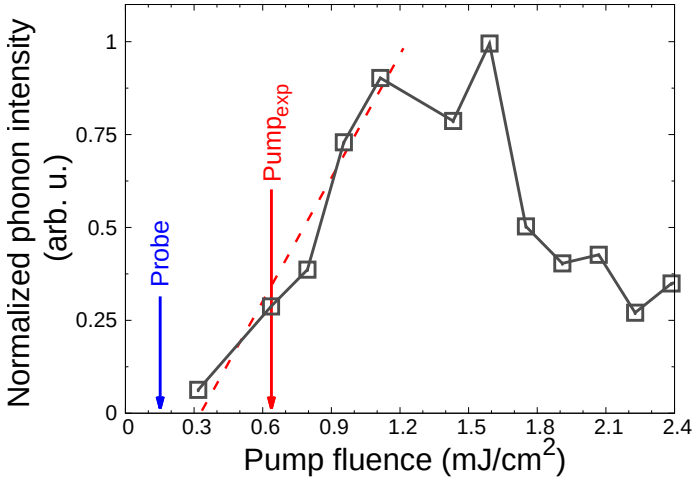

Figure S-4. Fluence dependence of the $\Delta R/R$ intensity of the B_1 mode with the pump laser. The fluence of the probe beam was set to 0.16 mJ/cm^2 (blue arrow). The red dashed line shows the approximately linear dependence, and the red arrow indicates the pump laser fluence used in the phonon lifetime measurements.

IV. LINEAR CHAIN MODEL FOR INTERLAYER MODES

The $2H$-$MoSe_2$ is a two dimensional material in which the atoms within each layer are connected by covalent bonds while the bulk crystal is formed by the stacking of these layers via van der Waals interactions. The interlayer shear (S) and the interlayer breathing (B) modes are characterized by the relative motion of the different layers but leaving the internal structure within each individual layer intact [3, 4]. The phononic properties of a multilayer $MoSe_2$ depend critically on the number of layers N and thereby, this makes Raman scattering a useful technique to characterize these two-dimensional materials [4–7].

Under a simple linear chain model to describe the shear and breathing modes, the atomic details within each layer are not necessary and are replaced by parameters that characterize the interlayer van der Waals interactions. As it is presented in figure S-5a, each layer of the material is replaced by an equivalent effective mass μ per unit area and a nearest-neighbouring interlayer force constant K per unit area. This approximation implies the substitution of the original layered crystal for a chain of effective masses. Since the acoustic modes do not imply the relative motions of atoms within each layer, each unit cell of the material could be analyzed as having two effective masses ($n_0 = 2$). It is clear that this approximation cannot describe the optical phonons of the system, that imply the relative motion of atoms within each layer.

Solving the elastic equation of motion for the linear chain model and accounting free surface (stress-free) boundary conditions, results the well known dispersion relation for the frequency of the modes as function of the number of

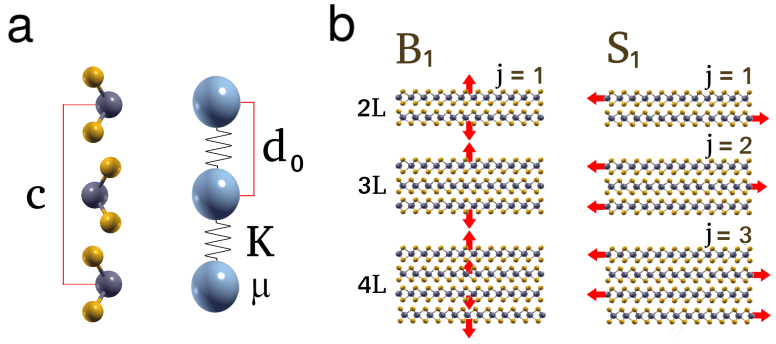

Figure S-5. **a)** linear chain model, each layer is replaced by an equivalent effective mass μ per unit area and a nearest-neighbouring interlayer force constant K per unit area. **b)** schematic of interlayer S_1 and B_1 modes for $N = 2, 3$ and 4, the arrows indicate the vibration direction of each rigid layer.

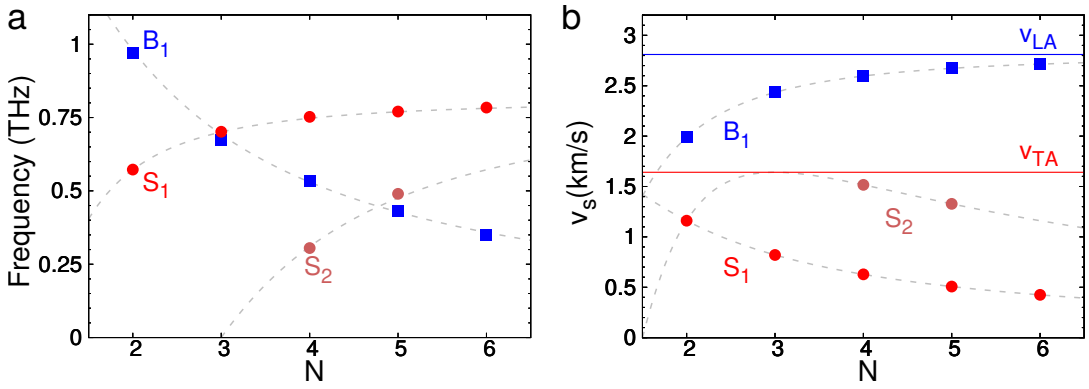

Figure S-6. **a)** B and S mode energies for Raman experiments performed for the thinner samples. **b)** calculated velocities for the corresponding B and S modes identified by Raman. The interpolation of the fitted values is shown with dashed grey lines and the blue(red) line is the bulk speed of sound for longitudinal(transversal) modes.

layers: [3, 4, 8]

$$f_{B(S)_{N,j}} = f_{B(S)_0} \sin\left(\frac{k_{N,j} d_0}{2}\right), \tag{1}$$

for the $B(S)$ mode. The interlayer distance is $d_o \simeq c/2$, where $c = 12.918\,\text{Å}$ is the bulk lattice parameter in the stacking direction [9, 10], $k_{N,j} = \frac{2\pi}{\lambda_{ac}}$ is the acoustic wavevector for the associated wavelength $\lambda_{ac} = \frac{2Nd_0}{j}$ and j the phonon branch index. $f_{B(S)_0}$ is related to the interlayer force constant per unit area $K_\perp(K_\parallel)$ and μ as

$$f_{B(S)_0} = \sqrt{\frac{K_{\perp(\parallel)}}{\pi^2 \mu}}. \tag{2}$$

The identification of the B and S modes in Raman scattering requires the measurements of polarized and cross-polarized Raman spectra. According to the Raman tensors, while the B mode could be observed only under parallel polarization measurements, the S mode is observed in both configurations [4]. Figure S-6a shows the B and S mode energies for Raman experiments performed in the thinner samples ($N = 2, 3, 4, 5$ and 6). The observed S_1 and S_2 modes belong to branches whose frequency increase with increasing N and correspond to the phonon branches $j = N - 1$ and $j = N - 3$ respectively. The B_1 mode instead belong to branches whose frequency decreases with increasing N and correspond to $j = 1$. This observations are in accordance with experiments performed in other TMDCs [4, 8]. Figure S-5b presents the schematics of interlayer S_1 and B_1 modes, the arrows indicate the vibration direction of each rigid layer.

The results presented in Fig. S-6a are fitted with the expression (1), where the only free parameter corresponds to f_{B_0} for the B mode and f_{S_0} for the S mode. The interpolation of this fitted curve is shown with dashed grey lines. The fitted values are $f_{B_0} = (1.39 \pm 0.03)\,\text{THz}$ and $f_{S_0} = (0.81 \pm 0.03)\,\text{THz}$. An estimation for the in-plain effective mass for each layer, accounting the atomic masses and the $MoSe_2$ in-plane unit cell [9, 10], results $\mu \simeq 4.41 \times 10^{-6}\,\text{kg/m}^2$. From the above fit, we can estimate using eqn.(2) the effective interlayer elastic force constants $K_\perp = 8.42 \times 10^{19}\,\text{N/m}^3$ and $K_\parallel = 2.85 \times 10^{19}\,\text{N/m}^3$. These values are of the order of those obtained for similar TMDCs 2D-systems [11, 12].

The acoustic propagation group velocity $v_{B(S)s}$ could be calculated from (1) applying the derivative with respect to the wavevector as $v_{B(S)s} = \frac{d\omega}{dk}$, and results

$$v_{B(S)s}(N, j) = \pi f_{B(S)_0} d_0 \cos\left(\tfrac{k_{N,j}\, d_o}{2}\right). \tag{3}$$

Figure S-6b shows the calculated velocities for the corresponding B and S modes identified by Raman. The dashed grey curves show the interpolation of eqn.(3). As the B and the S modes belong to different kind of branches, the regarding group velocity have different behaviour. The speed of sound along the stacking direction tends to the bulk speed of sound for the branch of index $j = 1$. For this reason, the v_B grows as function of N asymptotically to the value of the longitudinal acoustic velocity along the stacking direction (v_{LA}), while v_S decreases tending to zero when increasing N. The "bulk" longitudinal(transversal) acoustic velocity along the stacking direction $v_{LA}(v_{TA})$ could be obtained as a limit of $v_B(v_S)$ [eqn.(3)] for $j = 1$ and $N \to \infty$. The estimated "bulk" speed of sound are $v_{TA} = 1630\,\text{m/s}$ and $v_{LA} = 2820\,\text{m/s}$ (v_{ac} in the main text). The latter is in accordance with the pump-probe measurements (see main text, Fig. 3).

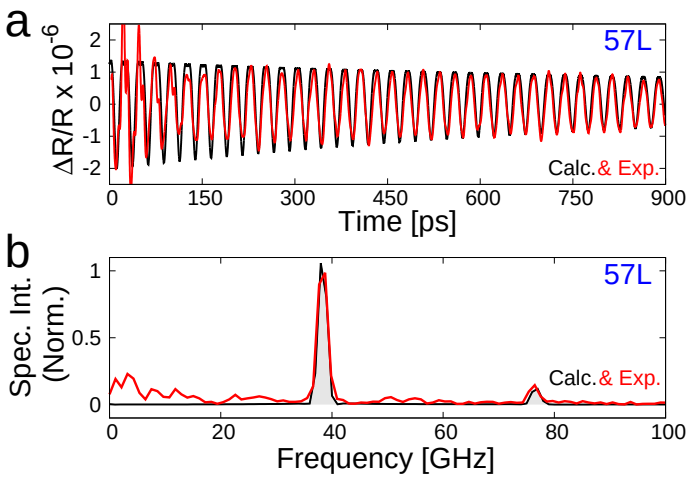

Figure S-7. **a)** Extracted oscillations (red curves) in the time-domain showing, corresponding to a 57L-$MoSe_2$ sample. **b)** Normalized numerical Fourier transform of the previous transient. The black curves are the simulations that best fit the experiments simultaneously in both domains.

V. PUMP-PROBE EXPERIMENTS IN THICK SAMPLES

By "thick samples" we mean thicknesses (d) of the flakes that are of the order or larger than the optical penetration depth

$$\delta_p = \frac{\lambda_{op}}{4\pi \Im m(\widetilde{n})}, \tag{4}$$

where $\lambda_{op} = 805\,\text{nm}$ is the central wavelength of the laser and $\widetilde{n}$ the complex refractive index taken from Ref.[13]. It is in these conditions that the model used for the simulations displays mayor advantages over an empirical function of the form $U(t) = A\exp(-t/\tau)\sin(2\pi f t + \phi)$, as it is usually used to derive the amplitude, frequency, and phase of the modes. The pump-pulse, roughly following its absorption profile, excites longitudinal acoustic strain pulses, which are launched into the sample. Analogously, the detection is thus sensitive to the presence of this propagating strain pulse within the volume given by the optical penetration depth of the probe laser [14, 15].

Such a propagating strain pulse, needs to be described as a certain superposition of the vibrational eigemodes of the flake (see Section IV). The important consequence is that the $\Delta R/R$ resulting from a combination of several modes cannot be described by the simple empirical $U(t)$ function, and mandatory needs to include the effect of the higher frequency modes that are excited within the flake. For consistency, we have used the *same* more complex model [16] that fully calculates $\Delta R/R$ to analyse all the measurements, and leaving the sample thickness (number N of layers) and the phonon lifetime (τ_{B_1}) as fitting parameters.

In what remains of this section we will show two cases where it becomes evident that the simple empirical $U(t)$ function fails to describe the observations: The first case corresponds to a $MoSe_2$ flake of $N = 57$L, leading to a thickness of $d = 36.8\,\text{nm}$ ($\delta_p \sim 100\,\text{nm}$). And the second, corresponds to the thickest $MoSe_2$ sample found, $N \simeq 519$L ($d = 335\,\text{nm} \gg \delta_p$), and basically behaves as "bulk" $MoSe_2$.

A. 57L $MoSe_2$

Between a thin flake and the bulk case, there are sample thicknesses that could not be catalogued in neither of these two groups. This is the case where the penetration depth is of the order of the $MoSe_2$ sample.

Figure S-7a shows the measurement (red) and the simulation (black) for a 57L $MoSe_2$ free-standing sample. After the first $\sim 150\,\text{ps}$, where the signal has kind of an irregular behaviour, the simulation has a relatively good agreement with the experiment. The nFT of this transient is presented in figure S-7b and the calculated curve is very well reproduced. Two peaks dominate the spectrum. The intense peak at $\sim$38 GHz corresponds to the fundamental confined mode, while the weaker one at $\sim$76 GHz to its second harmonic. This situation is clearly an intermediate one, where the penetration depth is of the order of the flakes thickness. Here the asymmetry of the induced initial stress is responsible for the generation of both, odd and even modes, as observed.

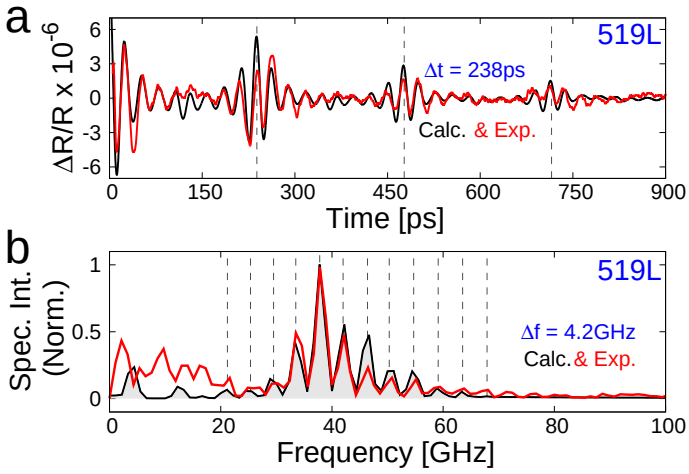

Figure S-8. **a)** phonon signal (red curves) in time-domain showing the extracted oscillations corresponding to a thick sample (519 layers $MoSe_2$). **b)** Numerical Fourier Transform of the corresponding transients. The black curves are the simulations that best fit the experiments simultaneously in both domains.

As we have chosen for the simulation the phonon lifetime proportional to $1/f$, the second harmonic mode at ∼76 GHz presents a faster relaxation time, that is observed in time domain for the lower times in the simulations and also in the measurement. In the spectral domain, the faster relaxation time for the higher frequencies is responsible for the intensity ratio between the peaks, that fits with the experiment. The value of $N = 57 \pm 2$ layers $MoSe_2$ together with the B_1 relaxation time $\tau = 1.52 \pm 0.03$ ns are critical for the fitting of this model. Note the excellent agreement of experiment and theory.

B. "Bulk" $MoSe_2$

Figure S-8a presents the extracted $\Delta R/R$ (red) in time domain for the pump-probe measurement of this sample. The signal does *not* correspond to a beating but to multiple reflections of the generated acoustic pulse at the flake's back and front surfaces of the sample, i.e. the $MoSe_2$-SiO_2 and the air-$MoSe_2$ interfaces. The acoustic pulse is generated at the flakes surface and propagates into the sample with a speed v_{LA}. As the pulse penetrates the sample, since the penetration of light decreases exponentially with depth, the detection is diminished (signal $\Delta R/R$ decreases). At around 124 ps the pulse gets reflected back at the back side of the sample and returns to the surface. By doing so, the acoustic pulse reenters the region where the probe laser is again sensitive to its detection ($\Delta R/R$ increases) [14]. At $t \simeq 248$ ps the acoustic pulse is reflected at the air-$MoSe_2$ interface and is again directed into the sample, were the process is repeated. It turns out that within this regime, the vibrational modes that are addressable have the frequencies described by [14]

$$f_b \simeq 2\, k_{op}\, v_{LA} \sim \frac{4\pi v_{LA} \Re e(\tilde{n})}{\lambda_{op}}, \tag{5}$$

where k_{op} is the optical wavevector of the probe laser. In the literature, the acoustic pulse are usually called "Brioullin" mode and is generated with the allowed frequency modes in the sample described by eqn.(1).

In the limit $N \gg 2$ the allowed modes within the sample are equi-spaced defining the *free spectral range* (the acoustic mode's separation) [17]

$$\Delta f = v_{LA}/(2d)\ , \tag{6}$$

where Δf matches the lower mode frequency (B_1) of 4.2 GHz. Figure S-8b presents the Fourier analysis of the signal shown on S-8a. The nFT basically shows a set of peaks with the frequency of the modes existing in the acoustic pulse and separated by $\Delta f = 4.2$ GHz, that according to eqn.(6) implies $d \sim 335$ nm $\simeq 519$ layers of $MoSe_2$.

In addition, considering the pulse travelling time of $\Delta t \sim 238$ ps within the samples, using the sound velocity obtained in section IV, one can estimate the thickness of this particular flake being

$$d = \tfrac{\Delta t}{2}\, v_{ac} \sim 333\,\text{nm} \simeq 516 \text{ layers } MoSe_2\ . \tag{7}$$

This value is reasonable and not far from the thickness obtained before.

The simulation of $\Delta R/R$ performed for this sample is presented in figure S-8 with black curves, and shows a good agreement with the experiment. The frequency modes and the multiple reflections of the acoustic pulse at the flake's surfaces of the sample are well reproduced in the temporal and spectral domain. As mentioned, the thickness of the $MoSe_2$ is a critical fitting parameter. Here we obtained $N = 519 \pm 5$ layers $MoSe_2$ and is also in accordance with the estimations above.

As is also evidenced here, the complex behaviour of the signal cannot be reproduced by the empirical function $U(t)$, and it is necessary to introduce the model for $\Delta R/R$ to correctly interpret the experimental results.

VI. DIFFERENT DAMPING MECHANISM CONSIDERED IN THE ACOUSTIC LIFETIME MODELLING

Three mechanism have been accounted for to describe the damping rate of the coherently generated B_1 modes in the $MoSe_2$ flakes. The first two involve the interaction of these mode with other *thermal* phonons of the sample at the given experimental temperature (subsections VI A and VI B); and the third, related to the losses due to surface effects when the samples gets thinner (subsection VI D).

A. Anharmonic 3-phonon scattering mechanism for the decay of phonons in anisotropic materials

The description of a crystal lattice accounting only a harmonic potential can not reproduce the phonon-phonon interaction, which provides one main mechanism responsible for the phonon decay in pure crystals. The relaxation time of a phonon due to three-phonon processes arises from the inclusion of *anharmonic* terms in the lattice Hamiltonian, casting away the concept of non-interacting phonons [18–20].

One model that captures the essence of these kind of three-phonon processes for calculating the acoustic decay times, based on a Landau-Rumer–type of approach [20–22], in combination with the single mode relaxation time (SMRT) approximation [18, 19, 23]. In particular, this approach using a Debye-type approximation proved to give reasonable results in similar systems for low frequency acoustic phonons [18, 19]. The conventional Debye model works fine for isotropic systems, where the velocities of sound are equal in all directions. Cases such as bulk one-dimensional Van der Walls crystals, e.g. bulk $MoSe_2$ or graphite, have quite different in-plane/out-of-plane velocities of sound and are thus anisotropic.

Based on the Debye model for anisotropic systems, proposed by Z. Chen, *et al.* in Ref.[24], we adapted the single mode relaxation time model in combination with a first order time-dependent perturbation to the anharmonic ionic potential [18, 19] to calculate the observed phonon damping time as function of its frequency.

The initial state of the phonon system is described by $|i\rangle = |n_{qs}, n_{q's'}, n_{q''s''}\rangle$, where q and s identify the wave vectors and polarizations of each phonon mode, respectively, and n_{qs} indicates the number of phonon in the state q, s. The anharmonic perturbation H_{anh} causes the system to scatter to a final state. Within a three-phonon process, two possibilities should be taken into account: First, the combination of two initial phonons to a third one (*class-I* process), i.e. $\omega_{q,s} + \omega_{q',s'} \rightarrow \omega_{q'',s''}$, case in which the final state is $|f\rangle = |n_{qs} - 1, n_{q's'} - 1, n_{q''s''} + 1\rangle$. And second, the annihilation of a phonon into two remaining (*class-II* process), i.e. $\omega_{q,s} \rightarrow \omega_{q',s'} + \omega_{q'',s''}$, where the final state is of the form $|f\rangle = |n_{qs} - 1, n_{q's'} + 1, n_{q''s''} + 1\rangle$ [18, 20]. Figure S-9a shows the Feynman diagrams for both processes. The rate of occurrence P_{3ph} of them, is given by Fermi's golden rule [18]

$$P_{3ph} = \frac{2\pi}{\hbar} \left|\langle f|H_{anh}|i\rangle\right|^2 \delta(E_f - E_i), \tag{8}$$

where the delta function ensures the conservation of energy between initial and final state.

Since our interest is centred at a state with an initial phonon with wavevector q and polarization state s (the B_1 longitudinal acoustic mode), its total single mode relaxation rate is proportional to P_{3ph}, and is given by [18]

$$\tau_{qs}^{-1} = \frac{\pi\hbar}{4\rho^3 N_0 \Omega} \sum_{q's'q''s''} \left|A_{qq'q''}^{ss's''}\right|^2 \frac{qq'q''}{v_s v_{s'} v_{s''}} \delta_{q+q'+q'',G} \left[\frac{\bar{n}_{q's'}(\bar{n}_{q''s''}+1)}{\bar{n}_{qs}+1} \delta(\omega_{qs} + \omega_{q's'} - \omega_{q''s''}) + \frac{1}{2} \frac{\bar{n}_{q's'}\bar{n}_{q''s''}}{\bar{n}_{qs}} \delta(\omega_{qs} - \omega_{q's'} - \omega_{q''s''}) \right], \tag{9}$$

where the first term within brackets corresponds to transitions of class-I, while the second term to transitions of class-II. $\bar{n}_{qs} = [\exp(\hbar\omega_{qs}/k_BT) - 1]^{-1}$ are the Bose-Einstein distribution functions for phonons in the state q,s and temperature T, G is a vector of the reciprocal lattice, N_0 the number of unit cells of volume Ω and density mass ρ, and the factor $\left|A^{ss's''}_{qq'q''}\right|^2$ is the three-phonon scattering strength of the anharmonic perturbation (H_{anh}) for the three-phonon process. Under some assumptions this strength can be approximated as a q independent magnitude, as [18]

$$\left|A^{ss's''}_{qq'q''}\right|^2 = \frac{4\rho^2}{\bar{v}^2}\gamma^2 v_s^2 v_{s'}^2 v_{s''}^2. \tag{10}$$

Here γ is the mode independent Grüneisen constant, $\bar{v}^2$ the phonon average group velocity and v_s, $v_{s'}$ and $v_{s''}$ the corresponding phonon group velocities for each of the involved acoustic phonon modes.

To evaluate eqn.(9) it is necessary to sum over all different phonon states q', s' and q'', s'' within the Brillouin zone. This involves the knowledge of the full acoustic phonon dispersion relation. In order to get more insight and understand the phenomenology underlying the involved processes, we follow the well known Debye approximation that states a linear dispersion relation for transverse and longitudinal phonon modes [18, 19]. It is important to mention that the Debye approximation is an approach that accounts for a strictly continuous Brillouin zone, and the modes in the flake's out-of-plane direction are in fact discrete. Consequently, it is expected to have a rather closer agreement with this model for thicker samples, i.e. where the acoustic free spectral range of the flake in the perpendicular direction is smaller, and for lower frequencies. Clearly, these kind of model excludes acoustic shear modes such as those present in atomically thin layered materials (e.g. Z-modes with parabolic dispersion relation). Being aware of these limitations, we intend to obtain a rather qualitative description that allows to get a better understanding of the processes involved in the decay of the coherently generated acoustic modes.

In an attempt to capture the essence of these kind of layered materials, we introduce the anisotropic Debye approximation [24]. A layered system such as the one we analyse in this work, has an important anisotropy, which is evidenced by the different velocity of sound in the in-plane direction ($v_\parallel$) and in the stacking (out-of-plane) direction ($v_\perp$). Neglecting the in-plane differences, the model proposes an ellipsoidal iso-energy as function of the wavevector q of the form

$$\omega^2_{q,s} = v^2_{\parallel,s} q^2_{\parallel,s} + v^2_{\perp,s} q^2_{\perp,s}, \tag{11}$$

where ω is the angular frequency of the acoustic phonon, $q_\parallel(q_\perp)$ the wavevector in the in-plane(out-of-plane) direction and $v_{\parallel,s}$ should be taken as an average of the in plane sound velocities for the polarization s.

Considering the relation given by eqn.(10), replacing the sum over q'' evaluating the Krönecker delta function, changing the sum over q' in eqn.(9) to $\sum_{q'} \rightarrow \frac{N_o\Omega}{8\pi^3}\int d^3q'$, expressing the integral in cylindrical coordinates $d^3q' \rightarrow q'_\parallel dq'_\parallel d\varphi_{q'} dq'_\perp$, and the anisotropic dispersion relation given by eqn.(11), we get

$$\begin{aligned}\tau^{-1}_{qs} = \frac{\hbar\gamma^2}{4\pi\rho\bar{v}^2}\sum_{s's''G}\int v_s v_{s'} v_{s''} q_{B_1} q' q'' \Bigg[&\frac{n_{q's'}(n_{q''s''}+1)}{n_{q_{B_1}s}+1}\delta(\omega_{q_{B_1}s} + \omega_{q's'} - \omega_{q''s''}) + \\ &\frac{1}{2}\frac{n_{q's'}n_{q''s''}}{n_{q_{B_1}s}}\delta(\omega_{q_{B_1}s} - \omega_{q's'} - \omega_{q''s''})\Bigg] q'_\parallel dq'_\parallel dq'_\perp \ ,\end{aligned} \tag{12}$$

where q in eqn.(9) was replaced by q_{B_1}, since it corresponds to the generated and observed B_1 mode that is a longitudinal acoustic mode (L_{B_1}) along the z direction.

The conservation of the momentum leads then to

$$q'' = \sqrt{q'^2_\parallel + (q_{B_1} \pm q'_\perp)^2}, \tag{13}$$

for the normal ($G = 0$) class-I (+) and class-II (-) processes. The Umklapp processes ($G \neq 0$) are discarded for reasons that will be explained later.

The integral over $q'_\parallel$ in eqn.(12) can be further evaluated by using the Dirac delta function through the substitution

$$\Delta = \omega_{q_{B_1}s} \pm \omega_{q's'} - \omega_{q''s''}, \tag{14}$$

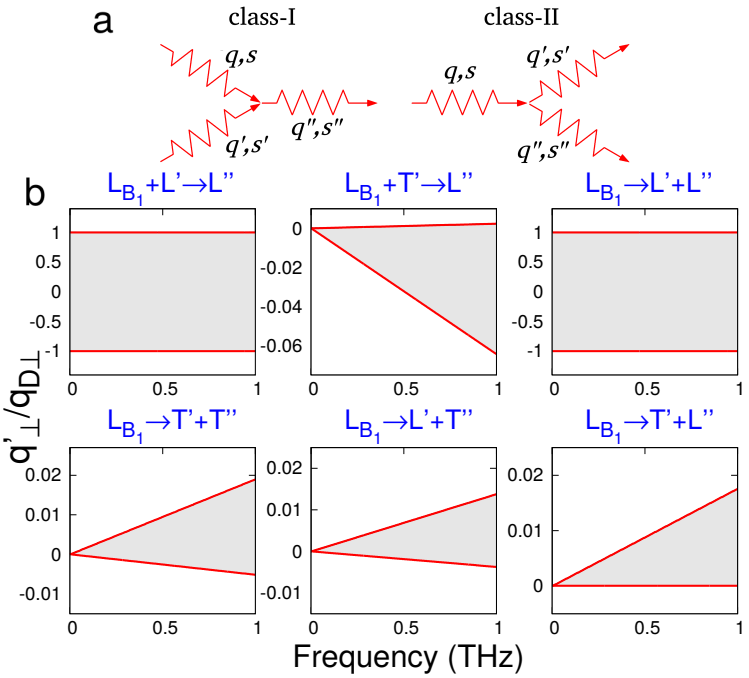

Figure S-9. **a)** Feynman diagrams for the class-I and class-II processes. **b)** areas that define the integration limits for eqn.(16), for the variable $q'_\perp/q_D$ as function of the L_{B_1} phonon frequency, for the different three-phonon processes.

leading to

$$d\Delta = \left(\pm \frac{d\omega_{q's'}}{dq'_\parallel} - \frac{d\omega_{q''s''}}{dq'_{\parallel}.} \right) dq'_\parallel \tag{15}$$

$\omega_{q''s''}$ depends on $q'_\parallel$ through the relation given by eqn.(13). Expression (12) reads then

$$\tau_{qs}^{-1} = \frac{\hbar\gamma^2}{4\pi\rho\bar{v}^2} \sum_{s's''} \int v_s v_{s'} v_{s''} q_{B_1} q' q'' \left[\frac{n_{q's'}(n_{q''s''}+1)}{n_{q_{B_1}s}+1} \frac{\omega_{q's'}\omega_{q''s''}}{v'^2_\parallel \omega_{q''s''} - v''^2_\parallel \omega_{q's'}} \right|_{q'_{\parallel 0}} - \frac{1}{2} \frac{n_{q's'} n_{q''s''}}{n_{q_{B_1}s}} \frac{\omega_{q's'}\omega_{q''s''}}{v'^2_\parallel \omega_{q''s''} + v''^2_\parallel \omega_{q's'}} \Big|_{q'_{\parallel 0}} \Bigg] dq'_\perp, \tag{16}$$

where $q'_{\parallel 0}$ is the value of $q'_\parallel$ that makes the argument of the Dirac delta functions in eqn.(12) zero, i.e. $\Delta = 0$. The explicit expression for $q'_{\parallel 0}$ depends on the class of process and the polarizations of the involved phonon modes.

It remains to be evaluated the limits of the integral (16) in $q'_\perp$. As the Debye approximation implies a cut-off frequency ω_D for acoustic waves in a crystal, in an anisotropic material it is possible to define the characteristic Debye frequencies of the plane ($\omega_{D\parallel}$) and perpendicular to the plane ($\omega_{D\perp}$) as [24],

$$\omega_{D\parallel} = v_\parallel q_{D\parallel}, \quad \omega_{D\perp} = v_\perp q_{D\perp}, \tag{17}$$

where $q_{D\parallel}(q_{D\perp})$ is the in-plane (perpendicular to the plane) cut-off wavevector. The ellipsoid

$$\frac{q_\parallel^2}{q_{D\parallel}^2} + \frac{q_\perp^2}{q_{D\perp}^2} = 1 \tag{18}$$

defines the cut-off wavevector for directions that are neither parallel nor perpendicular to the plane. The number density of the primitive cell (η) relates the total number of acoustic modes with the cut-off wavevectors as [24]

$$\eta = 3n_0/\Omega = \frac{1}{6\pi^2} q_{D\parallel}^2 q_{D\perp}, \tag{19}$$

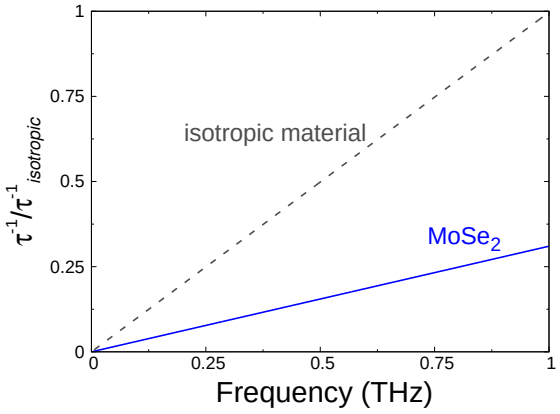

Figure S-10. Calculated phonon lifetime as a function of the frequency for $MoSe_2$, and the calculation for an equivalent isotropic material.

where n_0 is the number of effective masses in the unit cell and Ω its volume. As explained in section IV, $n_0 = 2$. The cut-off wavevector ellipsoid (18) is completely defined through (19) and the anisotropy ratio $q_{D\parallel}/q_{D\perp}$, that can be approximated by the extents of the first Brillouin zone in the corresponding directions [24],

$$\frac{q_{D\parallel}}{q_{D\perp}} = \frac{c}{a}, \tag{20}$$

where c (a) is the lattice parameter in the direction perpendicular (parallel) to the layers.

The limits in the integral (16) are determined by the possible real values of $q'_{\parallel}$ and $q'_{\perp}$ defined by the Dirac delta function ($\Delta = 0$) and by imposing that q' belongs to the cut-off wavevector ellipsoid.

From the different possible interactions giving raise to the B_1 mode's decay, only some of them need to be accounted for, namely: $L_{B_1} + L' \rightarrow L''$, $L_{B_1} + T' \longrightarrow L''$ for the class-I processes, and $L_{B_1} \longrightarrow L' + L''$, $L_{B_1} \longrightarrow T' + T''$, $L_{B_1} \longrightarrow L' + T''$, and $L_{B_1} \longrightarrow T' + L''$ for the class-II processes. L', L'' (T', T'') are the corresponding longitudinal (transversal) acoustic phonons involved in the three-phonon scattering processes.

Figure S-9b shows the areas that define the integration limits for the variable $q'_{\perp}$ in eqn.(16) normalized to $q_{D\perp}$. For a given B_1 mode frequency, the integration in $q'_{\perp}$ is constrained depending on the different possible interactions. Only the $L_{B_1} + L' \rightarrow L''$, and $L_{B_1} \longrightarrow L' + L''$ processes are limited by the cut-off wavevector ellipsoid and, since they are collinear ($q'_{\parallel} = 0$), the integration in $q'_{\perp}$ goes from -1 to 1. As these ranges of integration are much bigger than in the other processes, the main contribution to the phonon lifetime are due to them.

Different possible Umklapp processes that could be taken into account are: $L_{B_1} + T' \longrightarrow L''$ for the class-I processes, and $L_{B_1} \longrightarrow T' + T''$, $L_{B_1} \longrightarrow L' + T''$, and $L_{B_1} \longrightarrow T' + L''$ for the class-II processes [18]. However, the calculation shows that the Umklapp processes are not accessible since there are no q' that fulfil the energy and momentum conservation for the involved B_1 mode frequencies, as it was observed in Ref.[19] for an isotropic material.

For the calculations, the in-plane speeds of sound for bulk $MoSe_2$ were estimated from the simulated phonon dispersion relation from Ref.[25], where we derived $v_{\parallel L} \simeq 5800\,\mathrm{m/s}$ and $v_{\parallel T} \simeq 2900\,\mathrm{m/s}$ for the longitudinal and transversal velocities, respectively. For the out-of-plane components, we used the velocities estimated in the main text and in section IV. We perform the explicit evaluation of the integral in eqn.(16), including the processes sketched in Fig.S-9. The result for the inverse B_1 modes lifetime (τ^{-1}) for $MoSe_2$ is shown in Fig.S-10 (blue lines), and also in Fig. 4 of the main text. For the latter the proportionality factor was fitted to match the experimental data. Since many of the parameters involved are unknown (Grüneisen parameter, three-phonon scattering strength, etc.), τ^{-1} in Fig.S-9 is shown relative to the value obtained for an equivalent isotropic material, where the isotropic L and T speeds of sound are calculated as the average of those used for the $MoSe_2$: $\bar{v}_L = \frac{2}{3}v_{\parallel L} + \frac{1}{3}v_{\perp L} = 4800\,\mathrm{m/s}$ and $\bar{v}_T = \frac{2}{3}v_{\parallel T} + \frac{1}{3}v_{\perp T} = 2450\,\mathrm{m/s}$, and total averaged speed of sound is given by $\bar{v} = \frac{1}{3}\bar{v}_L + \frac{2}{3}\bar{v}_T$.

An important point to be mentioned is, that both calculated curves (anisotropic and isotropic) result *linear* with the frequency ($\tau^{-1} \propto f$). As many of the parameters included in the proportionality factor are unknown, it is not possible to compare both calculations with the measurements. It follows from Fig.S-10 that the anisotropic simulation gives scattering rates that are significantly lower than the isotropic equivalent, i.e. the lifetimes for the anisotropic system is increased with respect to the equivalent isotropic system. The reason for this is that, as explained before,

the mayor contributions to the lifetime comes from the collinear processes ($q'_{\parallel} = 0$). Its magnitude depends on the cut-off wavevector in this direction: $q_{D\parallel}$ for the anisotropic case, and q_D for the isotropic case. Since $q_D < q_{D\parallel}$, the lifetime is consequently increased for the anisotropic case.

B. Ahkieser-type mechanisms for the decay of phonons

The second approach considered to describe the acoustic decay rate of the coherently generated B_1 modes, is the Ahkieser–type mechanism [26]. In general this mechanism is usually described in terms of the attenuation (α_{ac}) of the generated mode propagating in the system as[20–22, 27, 28]

$$\alpha_{ac} = \frac{C_v T}{2\rho\, v_{ac}^3} \frac{\omega^2 \tau_{th}}{1+\omega^2\tau_{th}^2} (\gamma_{av}^{Ak})^2. \tag{21}$$

Using the fact that $\tau = (2\alpha_{ac} v_{ac})^{-1}$ [20], it is straight forward to get to the expression for τ_{Ak} displayed in the main text [see eqn.(6)]. This expression relies basically on two parameter that are not as simple to obtain experimentally, *i.e.* the mean lifetime of the thermal excitations (thermal phonon lifetime) τ_{th}, and the effective Grüneisen parameter, which is given as $(\gamma_{av}^{Ak})^2 = \langle\gamma^2\rangle - \langle\gamma\rangle^2$, and the $\langle ...\rangle$ brackets stand for thermal averages (see Refs.[20, 27] for details). Note, that the definition for γ_{av}^{Ak} is somehow different to the one described in eqn.(10).

C. Validity of both mechanism: 3-phonon *vs.* Akhiezer

In the accepted validity of the two above mentioned mechanism relies strongly on the observed modes frequency ($f = \omega/2\pi$), the analysed temperature (T), and the value for the thermal inter-phonon mean collision time or thermal phonon lifetime (τ_{th}).

It is generally accepted that the Akhiezer–type of ultra-/hyper-sonic attenuation is valid in the limit where [20–22]

$$\omega\,\tau_{th} \ll 1\ . \tag{22}$$

On the other hand, the Landau-Rumer–type of approach [20, 21], accounts for the quantum mechanical nature of the involved acoustic phonons. In general this approach is accepted to be valid when the mean free path (Λ_{th}) of the thermal phonons is larger than the acoustic wavelength (λ_{ac}) associated to the generated modes:

$$\Lambda_{th} > \lambda_{ac}\ . \tag{23}$$

Since $\Lambda_{th} = \bar{v}\tau_{th}$ (being $\bar{v}$ the average phonon velocity) and $\lambda_{ac} = \frac{2\pi}{\omega}\, v_{ac}$, the above expression is equivalent to [20–22]

$$\omega\,\tau_{th} > 1. \tag{24}$$

In order to roughly estimate the actual value of τ_{th}, for our particular case at room temperature, we use the expression for the thermal conductivity (κ) from the kinetic theory, $\kappa = \frac{1}{3} C_v \bar{v}^2 \tau_{th}$,[20–22] and values for the different parameters at room temperature ($T \approx 300\,\mathrm{K}$) which have been published in the literature.[29**?**] The estimated magnitude results

$$\tau_{th} \sim 3.3\,\mathrm{ps}. \tag{25}$$

Considering that the acoustic frequencies of the B_1 interlayer breathing modes are between 10^{10} and $10^{12}\,\mathrm{Hz}$, the product

$$\omega\,\tau_{th} = 2\pi f\,\tau_{th} \sim 0.2 - 20. \tag{26}$$

Hence, it is rigorously not possible to state the the limit $\omega\,\tau_{th} \ll 1$ (validity for the Akhiezer–type), and neither is it completely correct to consider the reciprocal case ($\omega\,\tau_{th} > 1$). As a consequence, we find our system to be at an intermediate transition region where $\omega\,\tau_{th} \simeq 1$. Under these circumstances we might incline towards the Landau-Rumer–type of approach. Several attempts for extending and matching both theoretical approaches have been tried.[21, 22] Although both mechanism rely on the same basic interaction, *i.e.* scattering with other thermal phonons, non of both extended descriptions have been quantitatively successful in accounting for the whole frequency range. Anyhow, these long-standing and intense debate and discussion is out of the scope of this work.

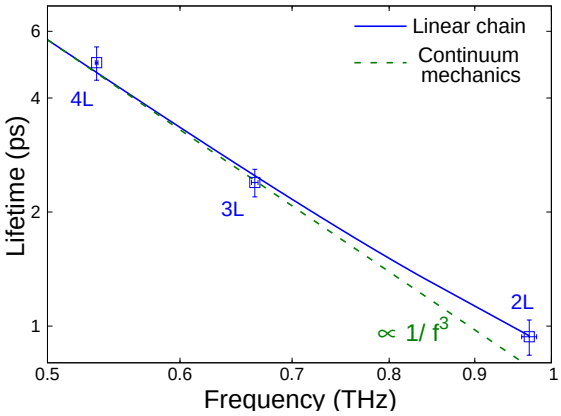

Figure S-11. Calculated relaxation time due to the boundary scattering for the linear chain model (blue) and the continuum mechanics model (dashed green line). The experimental data is shown with blue squares.

D. Surface roughness mechanism for the decay of phonons

The effect of the roughness on the phonon lifetime becomes more important when reducing the flake's thickness. In order to model this effect, we follow the approach of Ziman [30], described in the main text, that takes into account the surface *asperity* η and the associated imperfect (non specular) reflection of the acoustic wave at the flake's surfaces. The relaxation time due to the boundary scattering effects takes the form [19, 30]

$$\tau_b = \frac{N d_0}{v_s} \frac{1+p}{1-p}, \tag{27}$$

where $p(\lambda_{ac}) = \exp[-16\pi^2\eta^2/\lambda_{ac}^2]$ is the wavelength dependent specularity [19, 30].

Reordering (27), it is possible to express this contribution to the phonon lifetime as

$$\tau_b = \frac{\lambda_{ac}}{2v_s} \coth\left(\frac{8\pi^2\eta^2}{\lambda_{ac}^2}\right). \tag{28}$$

Within a continuum elastic limit, the acoustic pulse follows a linear dispersion relation. Under this approximation, as mentioned in the main text $v_s \to v_{ac}$, and the wavelength (λ_{ac}) of the acoustic phonons relates to its frequency as $\lambda_{ac} = v_{ac}/f$. Replacing this relation into eqn.(28) and assuming that the argument of the hyperbolic cotangent is small enough, the first order Taylor expansion yields

$$\tau_b \simeq \frac{v_{ac}^2}{16\pi^2\eta^2} f^{-3}. \tag{29}$$

Note that under these circumstances, the boundary contribution τ_b results proportional to f^{-3}. This rough approximation is used by some authors [19]. However, it is not entirely correct for our case, since the argument of the hyperbolic cotangent ($8\pi^2\eta^2/\lambda_{ac}^2$) is not small enough for the frequency region corresponding to the thinnest samples. In Figure S-11, the comparison between the calculation of τ_b with eqn. (28) and using (29) is shown, displaying the range where the difference between both expressions is more notorious. The continuous line is the one used in Fig.4 of the main text, and the dashed lines corresponds to the approximated expression. The blue squares are the experimental data, that correspond to 2L, 3L and 4L-$MoSe_2$. As observed the difference is small.

VII. ACOUSTIC QUALITY FACTOR

A parameter that is of interest for applications, e.g. for the optomechanics community is the quality factor ($\mathcal{Q}$-factor) of the system considered as a mechanical oscillator. The $\mathcal{Q}$-factor of such an oscillator, given the measured lifetimes as a function of the mode frequency, can be obtained by the simple expression:

$$\mathcal{Q} = \pi f \tau. \tag{30}$$

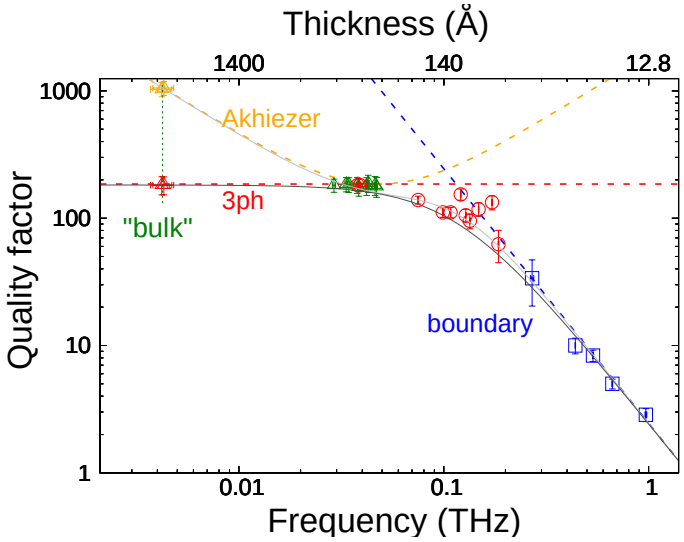

Figure S-12. Acoustic quality factor $\mathcal{Q}$ as a function of the B_1-mode frequency. The color coding is the same as the one displayed in Fig.2 and 4 of the main text.

Figure S-12 presents this magnitude for the measured membranes as a function of the frequency f of the B_1-mode calculated from the obtained modes' lifetime τ_{B_1} (see Fig. 4 in the main text), and eqn.(30). The colors for the experimental points and simulated lines coincide with those in Fig. 2 and 4 of the main text. The constant behaviour for lower frequencies when accounting the 3-phonon process results from the linear dependence with $1/f$ of the phonon lifetime τ_{3ph} in this frequency range, that cancels out with the multiplying f in eqn.(30). For the same reason, the Akhiezer process results in a linear dependence with $1/f$ for lower frequencies. For the thinner samples, in which the phonon decay is dominated by the boundary scattering and the phonon lifetime becomes $\tau \propto 1/f^3$, the $\mathcal{Q}$-factor is progressively reduced. Again, by means of Matthiensen's rule [30], the quality factors in the entire range are plotted with the grey lines. The $\mathcal{Q}$-factor obtained in this work, considering the range where the phonon lifetime depends as $1/f$ with the frequency, is of the order of those obtained for single crystalline silicon membranes in Refs.[31] and [19].

[1] Tae Young Jeong, Byung Moon Jin, Sonny H. Rhim, Lamjed Debbichi, Jaesung Park, Yu Dong Jang, Hyang Rok Lee, Dong-Hun Chae, Donghan Lee, Yong-Hoon Kim, Suyong Jung, and Ki Ju Yee. *ACS Nano*, **10**, 5560-5566, (2016). Coherent Lattice Vibrations in Mono- and Few-Layer WSe_2.

[2] Shaofeng Ge, Xuefeng Liu, Xiaofen Qiao, Qinsheng Wang, Zhen Xu, Jun Qiu, Ping-Heng Tan, Jimin Zhao, and Dong Sun. *Scientific Reports*, **4**, 5722, (2014). Coherent Longitudinal Acoustic Phonon Approaching THz Frequency in Multilayer Molybdenum Disulphide.

[3] Jianting Ji, Shan Dong, Anmin Zhang, and Qingming Zhang. *Physica E: Low-dimensional Systems and Nanostructures*, **80**, 130-141, (2016). Low-frequency interlayer vibration modes in two-dimensional layered materials.

[4] Liangbo Liang, Jun Zhang, Bobby G. Sumpter, Qing-Hai Tan, Ping-Heng Tan, and Vincent Meunier. *ACS Nano*, **11**, 11777-11802, (2017). Low-Frequency Shear and Layer-Breathing Modes in Raman Scattering of Two-Dimensional Materials.

[5] P. Soubelet, A. E. Bruchhausen, A. Fainstein, K. Nogajewski, and C. Faugeras. *Phys. Rev. B*, **93**, 155407, (2016). Resonance effects in the Raman scattering of monolayer and few-layer $MoSe_2$.

[6] Xin Lu, Xin Luo, Jun Zhang, Su Ying Quek, and Qihua Xiong. *Nano Research*, **9**, 3559-3597, (2016). Lattice vibrations and Raman scattering in two-dimensional layered materials beyond graphene.

[7] Alejandro Molina-Sánchez, Kerstin Hummer, and Ludger Wirtz. *Surface Science Reports*, **70**, 554–586, (2015). Vibrational and optical properties of MoS_2: From monolayer to bulk.

[8] Liangbo Liang, Alexander A. Puretzky, Bobby G. Sumpter, and Vincent Meunier. *Nanoscale*, **9**, 15340-15355, (2017). Interlayer bond polarizability model for stacking-dependent low-frequency Raman scattering in layered materials.

[9] Anupam Roy, Hema C. P. Movva, Biswarup Satpati, Kyounghwan Kim, Rik Dey, Amritesh Rai, Tanmoy Pramanik, Samaresh Guchhait, Emanuel Tutuc, and Sanjay K. Banerjee. *ACS Applied Materials & Interfaces*, **8**, 7396-7402, (2016). Structural and Electrical Properties of $MoTe_2$ and $MoSe_2$ Grown by Molecular Beam Epitaxy.

[10] R. Coehoorn, C. Haas, J. Dijkstra, C. J. F. Flipse, R. A. de Groot, and A. Wold. *Phys. Rev. B*, **35**, 6195–6202, (1987). Electronic structure of $MoSe_2$, MoS_2, and WSe_2. I. Band-structure calculations and photoelectron spectroscopy.

[11] Guillaume Froehlicher, Etienne Lorchat, François Fernique, Chaitanya Joshi, Alejandro Molina-Sánchez, Ludger Wirtz, and Stéphane Berciaud. *Nano Letters*, **15**, 6481-6489, (2015). Unified Description of the Optical Phonon Modes in N-Layer MoTe2.

[12] Yanyuan Zhao, Xin Luo, Hai Li, Jun Zhang, Paulo T. Araujo, Chee Kwan Gan, Jumiati Wu, Hua Zhang, Su Ying Quek, Mildred S. Dresselhaus, and Qihua Xiong. *Nano Letters*, **13**, 1007-1015, (2013). Interlayer Breathing and Shear Modes in Few-Trilayer MoS_2 and WSe_2.

[13] Yilei Li, Alexey Chernikov, Xian Zhang, Albert Rigosi, Heather M. Hill, Arend M. van der Zande, Daniel A. Chenet, En-Min Shih, James Hone, and Tony F. Heinz. *Phys. Rev. B*, **90**, 205422, (2014). Measurement of the optical dielectric function of monolayer transition-metal dichalcogenides: MoS_2, $MoSe_2$, WS_2, and WSe_2.

[14] C. Thomsen, J. Strait, Z. Vardeny, H. J. Maris, J. Tauc, and J. J. Hauser. *Phys. Rev. Lett.*, **53**, 989–992, (1984). Coherent Phonon Generation and Detection by Picosecond Light Pulses.

[15] C. Thomsen, H. T. Grahn, H. J. Maris, and J. Tauc. *Phys. Rev. B*, **34**, 4129–4138, (1986). Surface generation and detection of phonons by picosecond light pulses.

[16] M. F. Pascual-Winter, A. Fainstein, B. Jusserand, B. Perrin, and A. Lemaître. *Phys. Rev. B*, **85**, 235443, (2012). Spectral responses of phonon optical generation and detection in superlattices.

[17] Martin Grossmann, Matthias Klingele, Patricia Scheel, Oliver Ristow, Mike Hettich, Chuan He, Reimar Waitz, Martin Schubert, Axel Bruchhausen, Vitalyi Gusev, Elke Scheer, and Thomas Dekorsy. *Phys. Rev. B*, **88**, 205202, (2013). Femtosecond spectroscopy of acoustic frequency combs in the 100-GHz frequency range in Al/Si membranes.

[18] G. P. Srivastava. *The Physics of Phonons*. Adam Hilger, NY, 1st edition, 1990.

[19] J. Cuffe, O. Ristow, E. Chávez, A. Shchepetov, P-O. Chapuis, F. Alzina, M. Hettich, M. Prunnila, J. Ahopelto, T. Dekorsy, and C. M. Sotomayor Torres. *Phys. Rev. Lett.*, **110**, 095503, (2013). Lifetimes of Confined Acoustic Phonons in Ultrathin Silicon Membranes.

[20] Humphrey J. Maris. Interaction of sound waves with thermal phonons in dielectric crystals. In Warren P. Mason and R. N. Thurston, editors, *Physical Acoustics: Principles and Methods*, volume 8, chapter 6, pages 279–336. Academic Press, New York and London, 1st edition, 1971.

[21] P. G. Klemens. Effect of thermal and phonon processes on ultrasonic attenuation. In Warren P. Mason, editor, *Physical Acoustics: Principles and Methods*, volume 3 - part B, chapter 5, pages 201–234. Academic Press, New York and London, 1st edition, 1965.

[22] Rohn Truell, Charles Elbaum, and Bruce B. Chick. *Ultrasonic Methods in Solid State Physics*. Academic Press, 1st edition, 1969.

[23] Joseph Callaway. *Phys. Rev.*, **113**, 1046–1051, (1959). Model for Lattice Thermal Conductivity at Low Temperatures.

[24] Z. Chen, Z. Wei, Y. Chen, and C. Dames. *Phys. Rev. B*, **87**, 125426, (2013). Anisotropic Debye model for the thermal boundary conductance.

[25] S. Kumar and U. Schwingenschlögl. *Chemistry of Materials*, **27**, 1278-1284, (2015). Thermoelectric Response of Bulk and Monolayer MoSe2 and WSe2.

[26] A. Akhiezer. *J. Phys. USSR*, **1**, 277, (1939). On the Absorption of Sound in Solids.

[27] J.-Y. Duquesne and B. Perrin. *Phys. Rev. B*, **68**, 134205, (2003). Ultrasonic attenuation in a quasicrystal studied by picosecond acoustics as a function of temperature and frequency.

[28] B. C. Daly, K. Kang, Y. Wang, and David G. Cahill. *Phys. Rev. B*, **80**, 174112, (2009). Picosecond ultrasonic measurements of attenuation of longitudinal acoustic phonons in silicon.

[29] Bo Peng, Hao Zhang, Hezhu Shao, Yuchen Xu, Xiangchao Zhang, and Heyuan Zhu. *RSC Adv.*, **6**, 5767-5773, (2016). Thermal conductivity of monolayer MoS2, MoSe2, and WS2: interplay of mass effect, interatomic bonding and anharmonicity.

[30] J. M. Ziman. *Electrons and Phonons, The Theory of Transport Phenomena in Solids*. Oxford University Press, Oxford, 1st edition, 1960.

[31] A. Bruchhausen, R. Gebs, F. Hudert, D. Issenmann, G. Klatt, A. Bartels, O. Schecker, R. Waitz, A. Erbe, E. Scheer, J.-R. Huntzinger, A. Mlayah, and T. Dekorsy. *Phys. Rev. Lett.*, **106**, 077401, (2011). Subharmonic Resonant Optical Excitation of Confined Acoustic Modes in a Free-Standing Semiconductor Membrane at GHz Frequencies with a High-Repetition-Rate Femtosecond Laser.